Photocatalytic ozonation inactivation of bioaerosols by NiFeOOH nanosheets in situ grown on nickel foam

Haiyu Wang [a,b], Linghui Peng [a,b], Guiying Li [a,b], Weiping Zhang [a,b], Zhishu Liang [a,b], Huijun Zhao [c], Taicheng An [a,b,*]

[a] *Guangdong-Hong Kong-Macao Joint Laboratory for Contaminants Exposure and Health, Guangdong Key Laboratory of Environmental Catalysis and Health Risk Control, Institute of Environmental Health and Pollution Control, Guangdong University of Technology, Guangzhou 510006, China*
[b] *Guangzhou Key Laboratory of Environmental Catalysis and Pollution Control, Guangdong Technology Research Center for Photocatalytic Technology Integration and Equipment Engineering, School of Environmental Science and Engineering, Guangdong University of Technology, Guangzhou 510006, China*
[c] *Centre for Clean Environment and Energy, Griffith School of Environment, Gold Coast Campus, Griffith University, Queensland, 4222, Australia*

ARTICLE INFO

ABSTRACT

Inactivation of bioaerosols is critical to prevent the spread of microbial pathogens in air. Photocatalytic inactivation processes are environmental friendliness, while time-consuming and insufficient reactive oxygen species (ROSs) generation to irreversibly inactivate bacteria in bioaerosols. In this work, a novel photocatalytic ozonation (PCO) system was constructed, consisting of in situ grown NiFeOOH nanosheets on nickel foam (NiFeOOH NSs/NF) and trace concentration of ozone (O_3). Specifically, the PCO system exhibited remarkable photocatalytic inactivation efficiency (99.99%) within an ultrashort retention time of 8.07 s (RH = 90%) while no bacteria survived after 24-h cultivation. The irreversible inactivation of bacteria in this PCO system attributes to the synergistic effect of physical destruction by NiFeOOH NSs/NF and oxidative damage by photogenerated ROSs. This research provides a better alternative for efficient inactivation of bioaerosols and opens the door for the application of PCO system in reducing the exposure risk of bioaerosols.

1. Introduction

In recent years, bioaerosols have posed a great threat to human health, even affecting economic development and social stability [1–3]. The complicated pathogens in bioaerosols such as bacteria, viruses, fungal spores, biological fragments, and a variety of living particles can spread over long distances and remain alive for a long time, causing people infectious diseases, allergies, acute toxic reactions, and even death [4–8]. Typically, considerable cases of COVID-19 have been confirmed to be related to bioaerosols transmission, and this number is still growing rapidly [9–12]. Therefore, it is urgent to develop a high-efficiency bioaerosols inactivation system for reducing bioaerosols hazards.

In the past decades, photocatalytic technology has been considered as a promising approach for bioaerosols inactivation, owing to its eco-friendliness and low-cost [13–15]. Various semiconductor photocatalysts such as metal-organic frameworks (MOF) and titanium dioxide (TiO_2) have been developed and utilized in this field. For instance, Li et al. fabricated zinc-imidazolate (ZIF-8 MOF)-based air filters via hot pressing, obtaining 99.99% photocatalytic inactivation efficiency against *Escherichia coli* (*E. coli*) under simulated solar irradiation for 30 min [16]. Rodrigues-Silva et al. reported that the photocatalytic inactivation efficiency of TiO_2 (P25)-coated cellulose acetate for bacteria and fungi was about 88–93% [17]. Moreover, Lu et al. synthesized a hybrid of TiO_2 and monolayer $Ti_3C_2T_x$ nanosheet (MXene) catalyst coating on polyurethane (PU) foam with the photocatalytic inactivation efficiency of 99.9% against airborne *E. coli* under ultraviolet (UV) irradiation [18]. However, the photocatalysts coated on porous substrates cannot produce sufficient ROSs for irreversibly inactivating bacteria due to low light penetration into deep pores [19,20]. In this situation, the bacteria still survive in the deep pores and reproduce under suitable cultivation conditions, which causes secondary contamination [21,22].

Alternatively, photocatalytic ozonation (PCO) technology shows the potential to solve the above problems. It combines photocatalysis with O_3 to generate much more photogenerated ROSs, which may directly attack bacteria and cause damage to the cells [23–25]. Moreira et al.

found that the PCO coupling system of immobilized TiO_2 and O_3 can remove 99.99% of microorganisms in urban wastewater and surface water, which is more effective than individual photocatalysis [26]. Mecha et al. reported a TiO_2-based PCO process that can inactivate about 99.9% of waterborne pathogens within 15 min, shortening the contact time of 50–70% to irreversibly inactivate bacteria compared with the individual processes of O_3 and photocatalysis [27]. However, PCO technology still fails to meet the requirement of irreversibly inactivating bioaerosols due to slow ROSs oxidative damage. Inspired by the wings of insects such as cicadas and dragonflies that can inhibit, destroy, and even cause the death of bacteria due to their sharp nanostructures [28–31], researchers developed 0.04 mg/mL CuO nanosheets to inactivate bacteria in the aquatic phase with close to 100% reduction of bacteria [32]. This result demonstrates that the manipulation of the nanomaterial's shape can be a way to enhance the inactivation activity. Therefore, we supposed that introducing the physical destruction caused by nanostructures into PCO system can overcome the shortcoming of slow ROSs oxidative damage to bacteria [33,34], which may have great potential for bioaerosols inactivation.

In this study, we designed a high-efficient PCO system that combining of in situ grown NiFeOOH NSs/NF photocatalysts and trace concentration of O_3 (NiFeOOH NSs/NF/O_3). The PCO inactivation performance of NiFeOOH NSs/NF/O_3 was executed systematically. The growth of survival bacteria after inactivation process was evaluated by cultivating for 24 h. The mechanism of the synergistic effect of the physical destruction and oxidative damage in the NiFeOOH NSs/NF/O_3 system was proposed. This NiFeOOH NSs/NF/O_3 system exhibits integrated advantages of high efficiency and irreversible inactivation of bioaerosols, offering a promising alternative for reducing bioaerosols exposure risks.

2. Experimental section

2.1. Synthesis of NiFeOOH NSs/NF

NiFeOOH NSs/NF was prepared by a one-step hydrothermal method. Firstly, several pieces of nickel foam (NF) with a size of 2.5 cm × 2.5 cm were washed in an ultrasonic bath of acetone, 1 M hydrochloric acid, and running deionized water for 30 min, successively. After that, the samples were dried in a vacuum at 50 ℃. Secondly, the clean Ni foam was quickly placed in a 100 mL Teflon liner containing a mixed solution of 0.3 mM sodium sulfate and 0.3 mM iron (III) chloride hexahydrate with 80 mL H_2O. After 15 min of ultrasonication, it was transferred into an oven at 120 ℃ for 6 h. When the reaction is completed, the obtained samples (marked as NiFeOOH NSs/NF) were thoroughly washed with deionized water and dried at 60 °C for 24 h.

2.2. Materials characterization

The crystalline structure of the samples was characterized by X-ray diffractometer (XRD) (Rigaku Ultima IV) using Cu-Kα radiation. The morphology of the sample was obtained by scanning electron microscope (SEM) (Hitachi S-3400 N) at an accelerating voltage of 15 kV. The detailed preparation steps of SEM samples were provided in the Supporting Information. The surface morphology of the sample was measured by atomic force microscopy (AFM) (Bruker Dimension Icon). The light absorption spectra were recorded by UV-Vis diffuse reflectance spectrophotometer (UV-Vis DRS) at a wavelength range of 200–800 nm (UV 3600 Plus, Shimadzu, Japan). $BaSO_4$ was used as a reflectance reference for the UV–vis spectrophotometer. The specific surface area (S_{BET}) was measured by a surface area analyzer (Quantachrome, Autosorb-iQ). The photogenerated ROSs (•OH and •O_2^-) were detected by electron paramagnetic resonance (EPR) spectroscopy (Bruker A300 spectrometer) and 5,5-dimethyl-1-pyrroline N-oxide (DMPO) was used as the spin trapping reagent (www.eceshi.com).

2.3. Photocatalytic ozonation bioaerosols inactivation

2.3.1. Bioaerosols generation

E. coli (K 12) was used as a model bacterial strain to evaluate the inactivation efficiency of NiFeOOH NSs/NF/O_3. Firstly, the experimental strain *E. coli* was taken out from the cryopreservation and inoculated in Luria-Bertani (LB) broth at 37 °C for 12 h to obtain a bacterial suspension with a concentration of approximately 10^9 CFU/mL. Then, the above logarithmic phase bacterial suspension was centrifuged at 8000 rpm for 2 min and then resuspended in 0.9% NaCl solution for bioaerosols generation. A Collison six-jet nebulizer (BGI Inc., Waltham, MA) was used to generate bioaerosols. Then, the bioaerosols were balanced in a chamber with a volume of 50 L. The particle size of generated bioaerosols were characterized by an Anderson six-stage sampler. The diameter distribution of the generated bioaerosol particles are approximately 1 – 3 μm, shown in Fig. S1.

2.3.2. Bioaerosols sampling

In this study, a liquid sampler and an Anderson six-stage sampler were used to collect the bioaerosols from the reactor. The sampling medium was set as 10 mL of 0.9% NaCl solution. The sampling flow rate of the liquid sampler was 7–12.5 L/min. The sampling flow rate of the Anderson six-stage sampler was 28.3 L/min. The sampling volume was adjusted to 50 L. The collected samples (100 μL) were diluted and cultured on a nutrient agar plate at 37 °C for 18–24 h. Each experiment was repeated for three times.

2.3.3. Evaluation of bioaerosols inactivation performance

A schematic diagram of the experimental setup for bioaerosols inactivation was shown in Fig. S2. A photoreactor set up was connected to the outlet of the balancing chamber. A 20 W UV LED lamp (365 nm) was employed as a light source on the top of the quartz photoreactor (0.942 L). An O_3 generator (FQ-160, Beyok, China) was used to generate O_3 at a concentration of 0.1 ppm. The NiFeOOH NSs/NF was placed in the middle of the quartz reactor. We varied the retention time by controlling the sampling flow rate. The retention time was calculated using the following Eq. 1: Retention time (s) = Reactor Volume (L)/Flow rate (L/min). The parameters of the inactivation experiment were shown in Table S1. The bioaerosols from the outlet of balancing chamber and O_3 passed through the NiFeOOH NSs/NF from top to bottom. At last, the bioaerosols from the outlet were collected by the bioaerosols sampler. The PCO efficiency (η) was calculated using the following Eq. 2:

$$\eta = \frac{C}{C_0} \qquad (2)$$

where, C_0 (CFU/m^3) is the concentration of initial bioaerosols in air; C (CFU/m^3) is the concentration of bioaerosols after inactivation in air.

2.4. Cellular assay

2.4.1. Bacterial damage

Bacterial membrane damage was estimated at the cellular level through the release of lactate dehydrogenase (LDH), which indicates the membrane integrity of cells [35]. Therefore, the released LDH of collected bioaerosols were measured to reveal the cell damage of bioaerosols. After PCO inactivation, the bacteria were washed from NiFeOOH NSs/NF by 10 mL of 0.9% NaCl solution. Then 60 μL of LDH assay working fluid was added into 120 μL of the bacterial suspension. The mixture was incubated at 25 °C for 30 min. The samples were measured in a 96-well plate and the light absorbance at 490 nm was recorded via a microplate reader (Varioskan LUX; Thermo Fisher Scientific, USA). The detailed calculation of the LDH release was provided in the Supporting Information.

2.4.2. Bacterial oxidative stress response

The fluorescent probe DCFH-DA was used to monitor bacterial intracellular ROSs to reveal bacterial oxidative stress response. In detail, 1 μL of 1 mM DCFH-DA fluorescent probe (Beyotime Biotechnology) was added to 999 μL of the bacterial suspension eluted from NiFeOOH NSs/NF. Then the bacteria were incubated at 37 °C for 30 min in dark, and mixed every 5 min. Finally, a microplate reader (Varioskan LUX, ThermoFisher, USA) was used to measure the fluorescence intensity of the sample at 525 nm at an excitation wavelength of 488 nm.

2.5. The growth potential of survival bacteria after inactivation

The growth potential was assessed according to the method reported in previous studies [16,36]. Briefly, the bacteria were washed from NiFeOOH NSs/NF by 10 mL of 0.9% NaCl solution after PCO treatment, 10 μL of above bacterial eluent was cultured into sterile Luria-Bertani (LB) medium broth by shaking at 37 °C in dark. The growth curve of survival bacteria ($OD_{600\,nm}$) was monitored every hour by microplate readers (Varioskan LUX; Thermo Fisher Scientific, USA) in a 96-well plate. Meanwhile, the number of cultivated bacteria after PCO inactivation were counted by the standard plate count method. The 100 μL of the bacterial suspension was cultured on a nutrient agar plate at 37 °C for 24 h. Each experiment was repeated for three times.

3. Results and discussion

3.1. Characterization of NiFeOOH NSs/NF photocatalyst

The NiFeOOH NSs in situ grown on the surface of NF, and the NF serves as both the Ni source of NiFeOOH nucleus and the substrate of NiFeOOH NSs. As illustrated in Fig. 1a, the first step is the surface-redox of NF by Fe^{3+} to release Ni^{2+}. After that, the reduced Fe^{2+} and the released Ni^{2+} self-assembled in a weakly alkaline solution (Na_2SO_4 solution) to in situ grow NiFeOOH NSs on the surface of NF. It can be seen from a macroscopic view (right part of Fig. 1a), the uniform yellow appearance of the NiFeOOH NSs/NF comparing with pure NF indicates that the NiFeOOH NSs *in situ* grow evenly on the surface of NF. SEM images (Fig. 1b and c) and AFM image (Fig. S3) show that the thickness of NiFeOOH NSs is about 6 nm on the surface of NF. Ni, O and Fe elements distribution in NiFeOOH NSs/NF also confirms successful and uniform growth of NiFeOOH NSs on NF (Fig. 1d). The hole size of NF and NiFeOOH NSs/NF are both majorly distributed at 200 – 300 μm (Figs. S4 and S5). The specific surface area (S_{BET}) of NF and NiFeOOH NSs/NF did not change significantly (Table S2). Besides, the XRD pattern of NiFeOOH NSs/NF was also acquired. As shown in Fig. 1e, the diffraction peaks that correspond to the (003), (006), (012), and (110) planes of NiFeOOH NSs are displayed (PDF# 40–0215) [37], and the peaks located at 44.9°, 52.3° and 76.7° could be ascribed to the (111), (200),
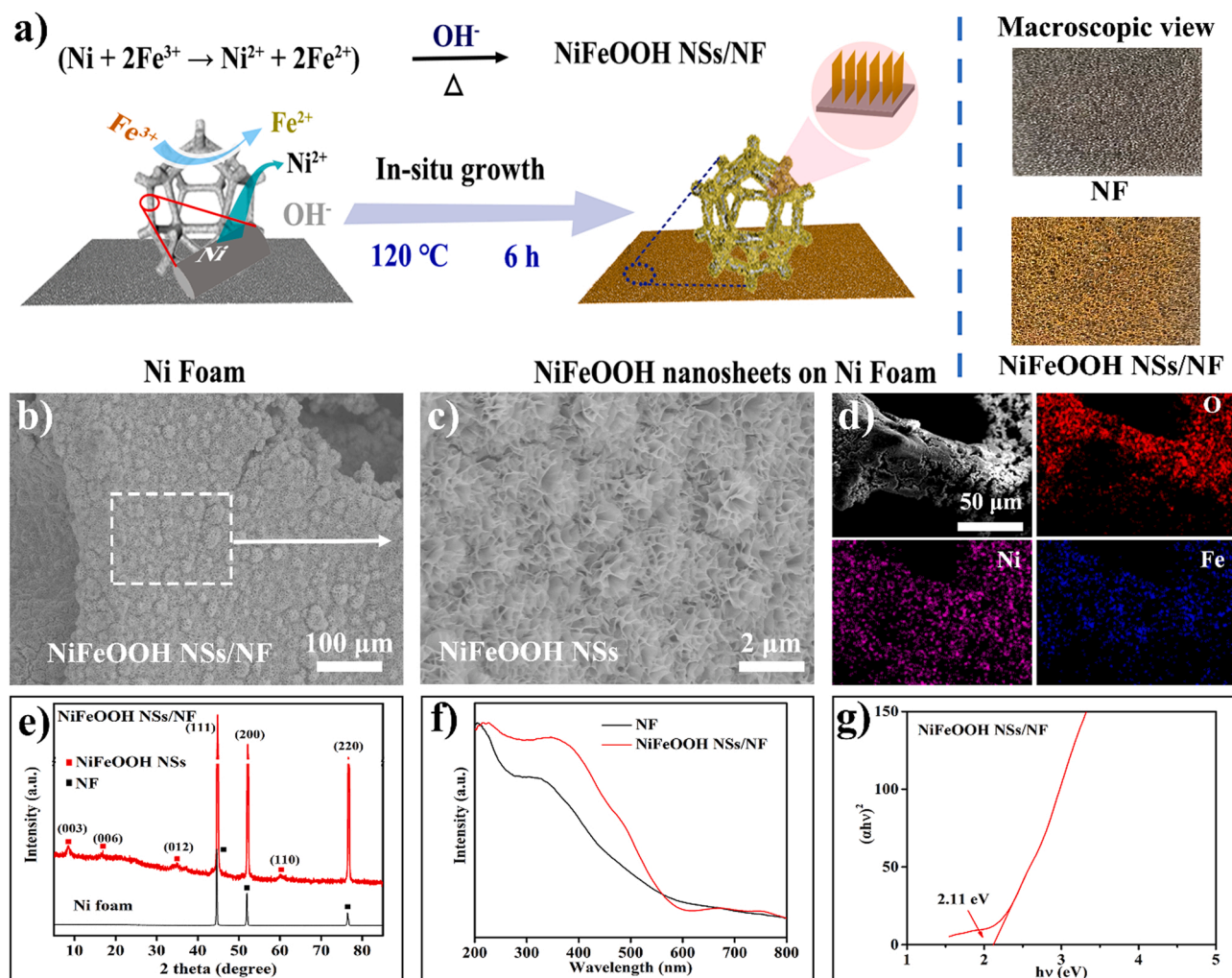

Fig. 1. a) Illustration of synthesis procedure of NiFeOOH NSs/NF. b) SEM images of NiFeOOH NSs/NF at low magnification and c) at high magnification. d) EDS elemental mapping images of NiFeOOH NSs/NF. e) XRD patterns of NF and NiFeOOH NSs/NF. f) UV–vis spectra of NF and NiFeOOH NSs/NF, and g) Bandgap of NiFeOOH NSs/NF.

and (220) planes of Ni (PDF# 04–0850) [38]. In short, the above results indicate that NiFeOOH NSs have successfully *in situ* grown on the surface of NF.

The optical properties and electronic band structure of NiFeOOH NSs/NF were measured to determine its photocatalytic activity. It can be seen from Fig. 1f, the light absorption of NiFeOOH NSs/NF is significantly stronger than that of NF, which means that NiFeOOH NSs/NF possesses higher light utilization. The band gap of NiFeOOH NSs/NF was derived using the Eq: $(\alpha h\nu)^n = C(h\nu - E_g)$. Here, α is the absorption coefficient, $h\nu$ is the incident photon energy, C is an energy independent constant, E_g is the bandgap energy, and n is the nature of transition. NiFeOOH NSs/NF is a direct bandgap semiconductor by calculation, the value of n is 2 [39,40]. As shown in Fig. 1g, the bathochromic shift of absorption edge endows NiFeOOH NSs/NF with a bandgap of E_g = 2.11 eV. Photogenerated carriers will be generated when the photocatalyst absorbs photon energy larger than its E_g. Thus, NiFeOOH NSs/NF here is very easily excited by UV LED lamps with a wavelength of 365 nm and it is very beneficial to the photocatalytic performance [34]. In summary, the above characterizations confirm that NiFeOOH NSs/NF photocatalysts studied here with suitable band gap and efficient light utilization.

3.2. Evaluation of bioaerosols inactivation efficiency

The bioaerosols inactivation performance of O_3, NiFeOOH NSs/NF, and NiFeOOH NSs/NF/O_3 in dark and under UV irradiation were comparatively investigated and retention time was 8.07 s. As depicted in Fig. 2a, the bioaerosols inactivation efficiency of O_3 is only 1.90% in dark and 3.8% under UV irradiation, eliminating the inactivation effect by O_3. For NiFeOOH NSs/NF, the bioaerosols inactivation efficiency increases from 30.80% (in dark) to 87.80% (under UV irradiation). This result shows that NiFeOOH NSs/NF possesses photocatalytic inactivation under UV irradiation. The inactivation efficiency of NiFeOOH NSs/NF/O_3 in dark is 61.40%, which is higher than O_3 and NiFeOOH NSs/NF individually. Significantly, the inactivation efficiency of NiFeOOH NSs/NF/O_3 reaches about 99.99% under UV irradiation, which is obviously higher than that of NiFeOOH NSs/NF and O_3, respectively. This PCO system shows superior performance compared with previous works (Table S3). The results tell the fact that the inactivation performance of NiFeOOH NSs/NF/O_3 processes superior high bacterial inactivation efficiency among NiFeOOH NSs/NFs, O_3, and NiFeOOH NSs/NF/O_3 under UV irradiation.

The influence of retention time on bioaerosols inactivation efficiency of NiFeOOH NSs/NF/O_3 was investigated. As shown in Fig. 2b, the inactivation efficiency of NiFeOOH NSs/NF/O_3 under UV irradiation increases with prolonged retention time. The inactivation efficiency is 67.99% at 1.99 s, and then increases to 99.78% when retention time is 4.52 s. A maximum inactivation efficiency reaches up to 99.99% when the retention time is 8.07 s. It can be easily explained by the fact that the long retention time of airflow may offer more direct contact chances between bacteria and photocatalyst and more ROSs generation, improving the inactivation efficiency [41,42]. However, to obtain a reasonable balance between air volume and disinfection efficiency in PCO process, we chose the retention time of 8.07 s for the study.

Apart from retention time, the impact of RH on bioaerosols inactivation of NiFeOOH NSs/NF/O_3 was also evaluated. As shown in Fig. 2c,
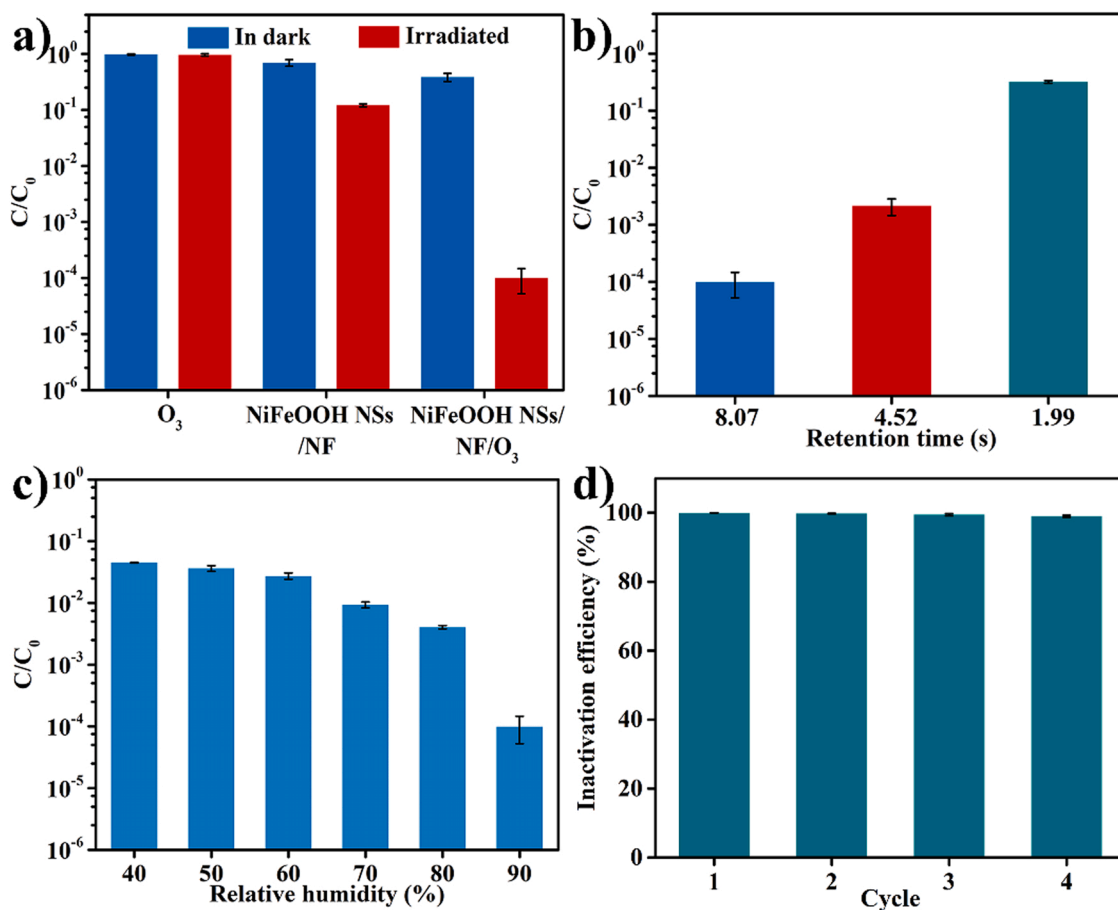

Fig. 2. a) Comparison of the bioaerosols inactivation efficiency of O_3, NiFeOOH NSs/NF, and NiFeOOH NSs/NF/O_3 in dark and under UV irradiation (RH=90%, retention time = 8.07 s). b) Effect of retention time on bioaerosols inactivation efficiency (RH=90%), c) Effect of relative humidity on bioaerosols inactivation efficiency (retention time = 8.07 s), d) The reusable stability of NiFeOOH NSs/NF/O_3 for bioaerosols inactivation (RH=90%, retention time = 8.07 s).

the photocatalytic inactivation efficiency rises with increasing RH. When the RH of the reaction system is between $40 \pm 3\%$ – $60 \pm 3\%$, the photocatalytic bioaerosols inactivation efficiency of NiFeOOH NSs/NF/O_3 are only 95.50–97.25%. However, the inactivation efficiency reaches a maximum value of 99.99% at RH of $90 \pm 3\%$. The reason may be that high RH is beneficial for the NiFeOOH NSs/NF catalyzing the reaction of O_3 and water vapors to generate ROSs under UV irradiation [43–45]. In addition, the cell membrane of bacteria may swell and become thin in such high RH (90%), resulting in easier inactivation of the bacteria [46]. Noticeably, the NiFeOOH NSs/NF/O_3 system still keeps sufficient inactivation efficiency after being continuously used under UV irradiation for several times (Fig. 2d). The intensity of light irradiation can affect the inactivation efficiency (Fig. S6). To balance energy consumption and inactivation efficiency, we chose lower power (20 W) in the following study. In summary, the NiFeOOH NSs/NF/O_3 system is high-efficiency, reusable and stable for long-term bioaerosols inactivation at high RH and short retention time.

3.3. Mechanism of bioaerosols inactivation

3.3.1. Photocatalytic oxidative damage

In the NiFeOOH NSs/NF/O_3 system, oxidative damage caused by photogenerated ROSs is an important pathway in the process of bioaerosols inactivation. Because photogenerated ROSs such as $\bullet OH$ and $\bullet O_2^-$ can strongly attack various bacterial cellular tissue [47]. To verify the photogeneration of ROSs in the NiFeOOH NSs/NF/O_3 system, EPR measurements were conducted with and without introducing O_3 under UV irradiation. As shown in Fig. 3a, the characteristic peaks of $\bullet OH$ with the intensity of 1: 2: 2: 1 appear when NiFeOOH NSs/NF without O_3 was excited by UV light. It tells that the NiFeOOH NSs/NF with efficient light utilization and a suitable bandgap ($E_g = 2.11$ eV) can promote electron transfer and generate ROSs under UV irradiation [25]. Interestingly, the characteristic peaks of $\bullet OH$ in NiFeOOH NSs/NF/O_3 are found to be around twice higher than that of without O_3. Meanwhile, the characteristic peaks of $\bullet O_2^-$ in NiFeOOH NSs/NF/O_3 also show the same increasing trend (Fig. 3b). These results are strong indications that more $\bullet OH$ and $\bullet O_2^-$ are generated in the NiFeOOH NSs/NF/O_3 system. In NiFeOOH NSs/NF photocatalytic reaction process, ROSs are generated from H_2O_2-mediated three-electron-reduction route, resulting in a relatively low yield of ROSs, while for NiFeOOH NSs/NF/O_3 system, ROSs also can be generated from additional $\bullet O_3^-$-mediated one-electron-reduction pathway [34]. Moreover, O_3 ($E(O_3) = 2.07$ V vs NHE) possesses a higher oxidation potential than O_2 ($E(O_2) = 1.23$ V vs NHE), resulting in easier thermodynamically capture of photogenerated electrons by O_3 in this process [48]. Therefore, trace O_3 significantly improves the ROSs generation in the NiFeOOH NSs/NF/O_3 system, leading to a high effecient inactivation performance of it.

3.3.2. Physical destruction of bacteria

In order to figure out whether physical destruction exists in the NiFeOOH NSs/NF/O_3 system, we also prepared NiFeOOH nanoparticles on NF (NiFeOOH NPs/NF) that without sharp edge for physical destruction as a comparison. The UV–vis spectra, SEM images and XRD patterns of NF and NiFeOOH NPs/NF were shown in Figs. S7-S10, indicating that irregular NiFeOOH NPs grow uniformly on the surface of NF and optical properties and crystal structure of NiFeOOH NPs/NF are similar to that of NiFeOOH NSs/NF. The morphology of the NiFeOOH NPs shows blunt round shape without sharp edge, while that of NiFeOOH NSs is sharp. As shown in Fig. 4a, we found that the inactivation efficiency of NiFeOOH NSs/NF with sheet shape is about 30.34% in dark, which is about 19% higher than that of NiFeOOH NPs/NF with round shape under the same condition. As illustrated in Fig. 4b, we hypothesize that the high inactivation efficiency of NiFeOOH NSs/NF comes from the sharp edges of nanosheets scratching and inserting into the cell membrane of the bacteria during contact. On the contrast, NiFeOOH NPs with blunt round shape can only contact with bacteria.

To verify this hypothesis of physical damage, the bacteria after being treated with NiFeOOH NSs/NF and NiFeOOH NPs/NF in dark were observed by SEM. It can be seen in Fig. 4c that the shape of some bacteria collapsed after being treated with NiFeOOH NSs/NF. In addition, the high-resolution SEM image (Fig. 4d) further illuminated that cell membrane of bacteria with irregular shape on NiFeOOH NSs, indicating NiFeOOH NSs/NF can induce physical destruction and lysis of bacteria. On the other hand, the morphological structure of the bacteria is relatively complete after being treated with NiFeOOH NPs/NF and NF (Figs. 4e, 4 f and S11). It shows that NiFeOOH NPs/NF with round shape cannot cause significant physical damage to bacteria, which is consistent with its lower inactivation efficiency. The degree of bacterial destruction may be exacerbated by the increasing sharpness of the nanostructure [49], thus, NiFeOOH NSs cause 19% higher inactivation efficiency than NiFeOOH NPs. These results indicate that the sharp nanosheets structure of NiFeOOH NSs/NF may be more likely to cause physical destruction to bacteria than that of NiFeOOH NPs/NF.

3.3.3. Synergistic effect of physical destruction and oxidative damage

In NiFeOOH NSs/NF/O_3 system, both physical destruction and oxidative damage contribute to the high efficiency of bioaerosols inactivation. However, we found that the inactivation performance of NiFeOOH NSs/NF/O_3 system is not a simple accumulation of physical destruction and oxidative damage (discussed in 3.2), indicating that the synergistic effect of them may play a key role. Therefore, the synergistic effect of NiFeOOH NSs/NF/O_3 was further revealed from the cellular level. We monitored the oxidative stress response of survival bacteria after being inactivated by NiFeOOH NSs/NF and NiFeOOH NSs/NF/O_3 under UV irradiation. It can be seen from Fig. 5a that the bacteria
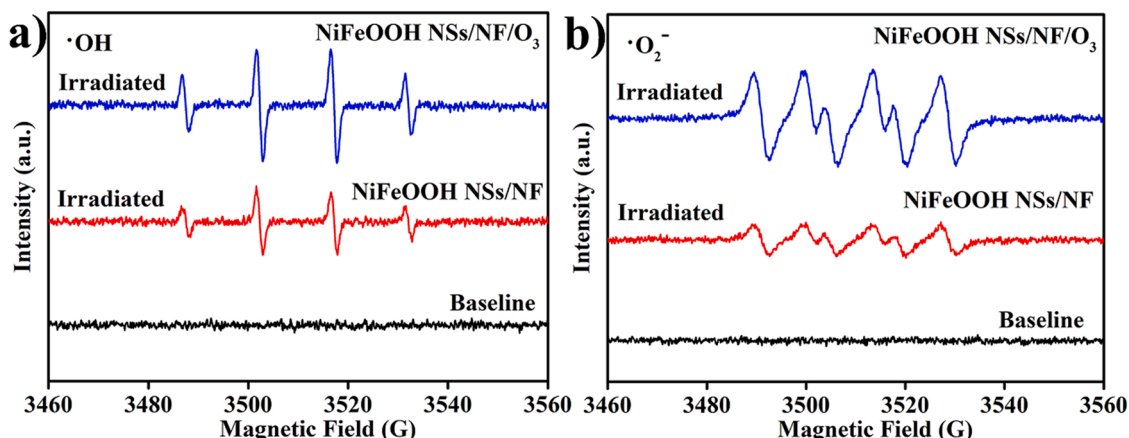

Fig. 3. Comparison of DMPO spin-trapping EPR spectra of NiFeOOH NSs/NF and NiFeOOH NSs/NF/O_3 under UV irradiation. a) $\bullet OH$ and b) $\bullet O_2^-$.
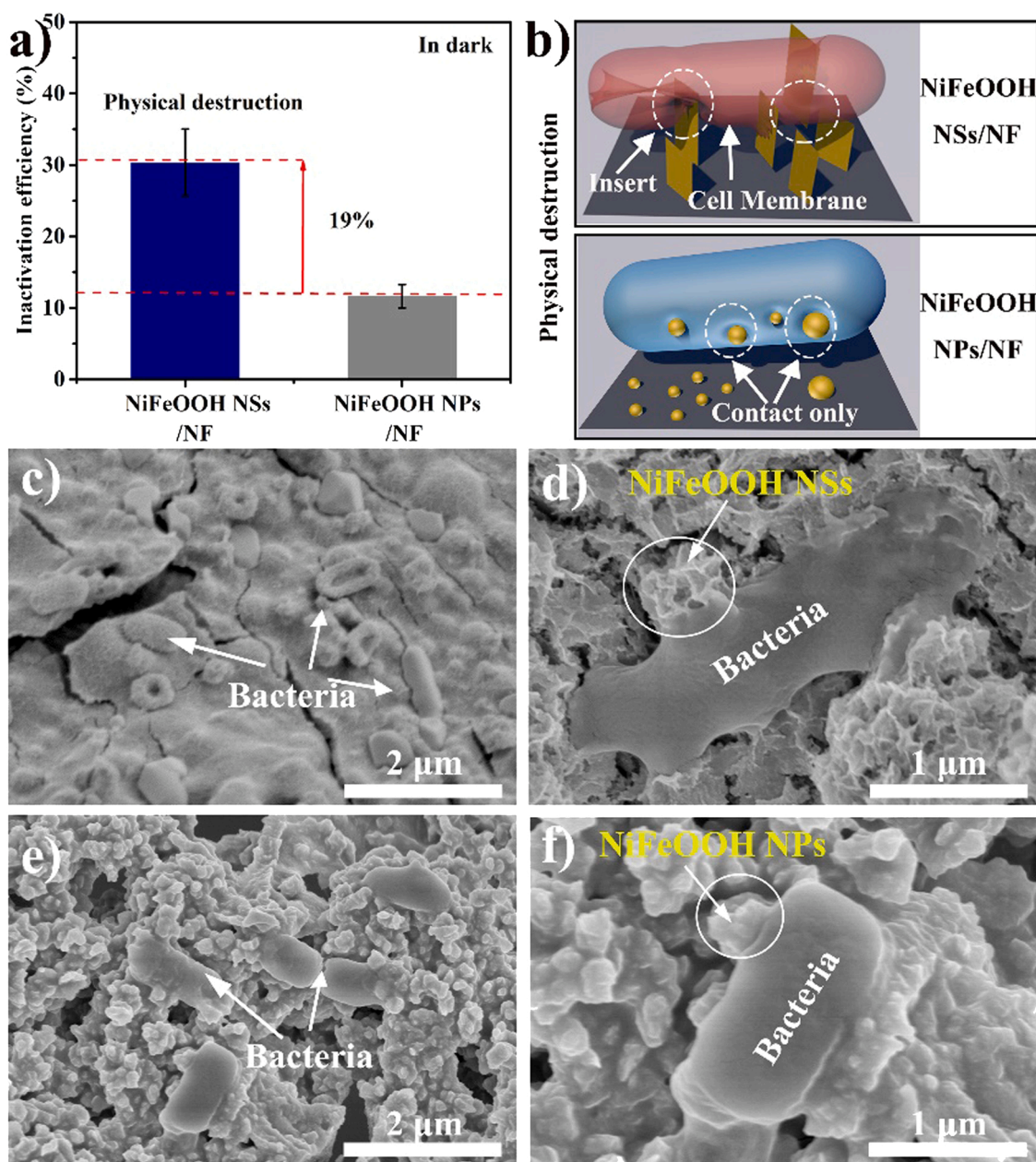
Fig. 4. a) Comparison of the bioaerosols inactivation efficiency of NiFeOOH NSs/NF and NiFeOOH NPs/NF in dark. b) Illustration of bacterial physical destruction caused by NiFeOOH NSs/NF and NiFeOOH NPs/NF. SEM images of the physical destruction of the bacteria after being inactivated with NiFeOOH NSs/NF in dark c) at low magnification and d) at high magnification. SEM images of the physical destruction of the bacteria after being inactivated with NiFeOOH NPs/NF in dark e) at low magnification and f) at high magnification.

produce ~3 times higher levels of intracellular ROSs after being treated by NiFeOOH NSs/NF/O_3 than by NiFeOOH NSs/NF, which indicates that the NiFeOOH NSs/NF/O_3 treatment induces much stronger oxidative stress in bacteria than without O_3. When introducing O_3 into the system, more photogenerated ROSs attack bacteria, causing more intracellular ROSs generation. It is widely accepted that the high intracellular ROSs can oxidize the macromolecules in the cell, disrupt their normal function and cause damage to the cell or even death [31]. Therefore, we can conclude that the ROS photogenerated by NiFeOOH NSs/NF/O_3 can stimulate bacteria to produce higher intracellular ROSs, which may enhance bacteria inactivation.

Moreover, the destruction level of bacteria after being inactivated by NiFeOOH NSs/NF/O_3 and NiFeOOH NSs/NF were further analyzed by quantifying LDH release, because the release of LDH is regarded as an important indicator of cell membrane integrity. As shown in Fig. 5b, the

LDH enzyme release of bacteria is only 29% in NiFeOOH NSs/NF without O_3, demonstrating the slight physical destruction from nanosheet and weak oxidative damage. In the contrast, the bacteria exhibit 80% release of LDH enzyme after being inactivated by NiFeOOH NSs/NF with O_3, which indicates more bacterial cell membranes were destroyed when introducing O_3. This result also suggests that introducing O_3 is benefit for physical destruction. In short, the intracellular ROS generation and high LDH enzyme release of bacteria signify the synergistic effect of physical destruction and oxidative damage that can cause bacterial ROS level increase and loss of cell membrane integrity during NiFeOOH NSs/NF/O_3 photocatalytic inactivation.

The growth curves of survival bacteria after being inactivated by NiFeOOH NSs/NF and NiFeOOH NSs/NF/O_3 under UV irradiation demonstrated irreversible inactivation of the NiFeOOH NSs/NF/O_3 system. As shown in Fig. 5c, the growth curves of survival bacteria show
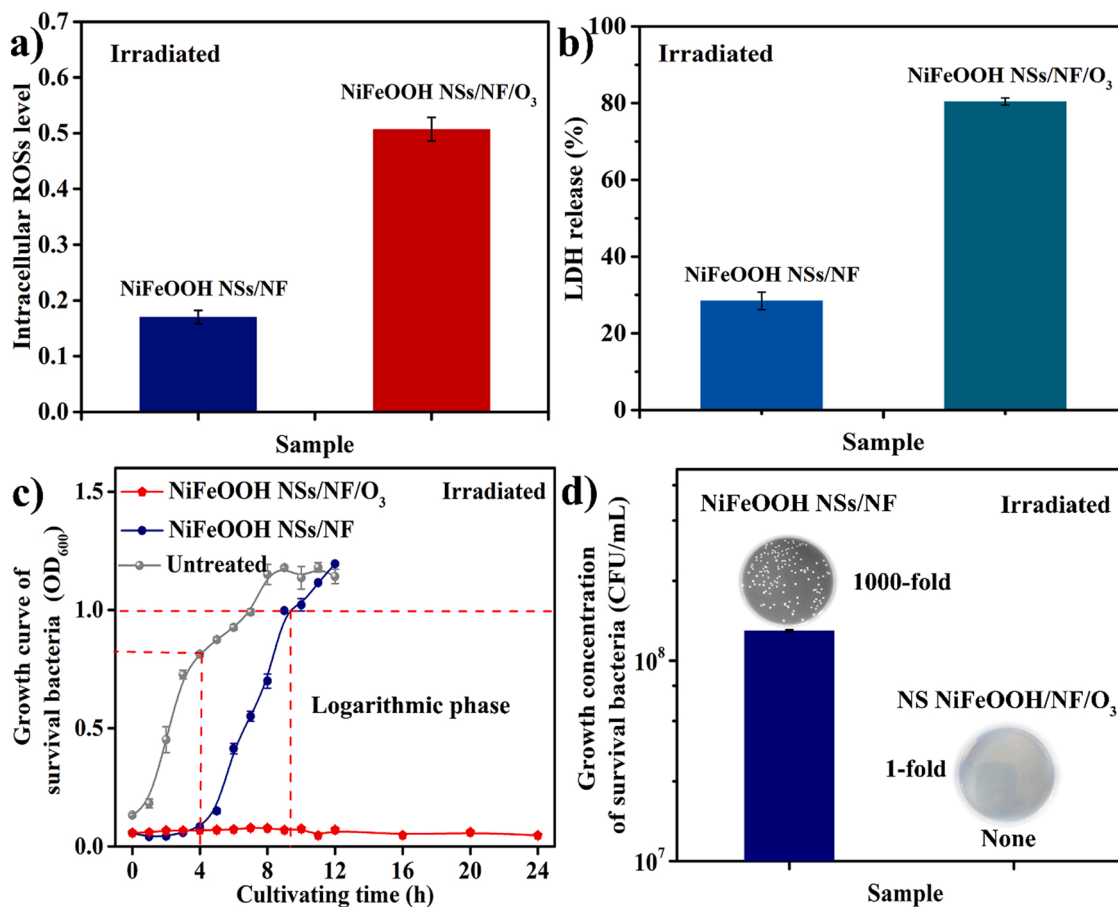
Fig. 5. a) The intracellular ROSs of bacteria after being inactivated with NiFeOOH NSs/NF and NiFeOOH NSs/NF/O$_3$ under UV irradiation. b) The LDH release of bacteria after being inactivated with NiFeOOH NSs/NF and NiFeOOH NSs/NF/O$_3$ under UV irradiation. c) The growth curves of survival bacteria after being inactivated with NiFeOOH NSs/NF and NiFeOOH NSs/NF/O$_3$ under UV irradiation, b) The growth concentration of survival bacteria after being inactivated with NiFeOOH NSs/NF and NiFeOOH NSs/NF/O$_3$ under UV irradiation.
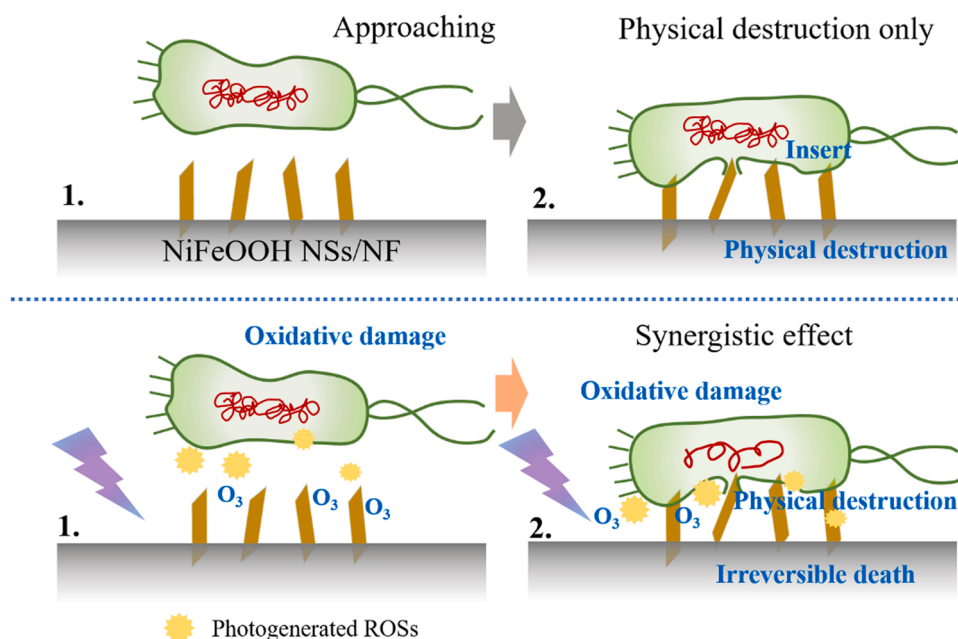
Scheme 1. Illumination of proposed mechanism of NiFeOOH NSs/NF/O$_3$ PCO system.

obviously different trends after being inactivated by NiFeOOH NSs/NF with and without O_3 under UV irradiation. Survival bacteria treated by NiFeOOH NSs/NF without O_3 under UV irradiation show a faster growth rate and the OD $_{600\,nm}$ rapidly reaches 1.2 ± 0.01 within 12 h. These bacteria rapidly enter the logarithmic growth phase may be related to the slight physical damage of bacteria caused by NiFeOOH NSs/NF and weak photocatalytic oxidation damage [50,51]. However, after being inactivated with the NiFeOOH NSs/NF/O_3, the OD $_{600\,nm}$ value was 0.05 ± 0.01 even after 24 h of incubation and no colonies were also counted by the standard plate count method (Fig. 5d). This result gives strong evidence of introducing trace O_3 into NiFeOOH NSs/NF significantly enhances damage to bacteria. The reason may be that the sharp nanosheets of NiFeOOH NSs/NF combine with O_3 make irreversible damage to bacteria, preventing their repair and growth even under suitable circumstances.

Hence, based on the results discussed above, the inactivation mechanism of the NiFeOOH NSs/NF/O_3 system was proposed. The whole process of PCO based on the NiFeOOH NSs/NF/O_3 was shown in Scheme 1. In this system, if no light involved in (no PCO involved), bacteria in the bioaerosol go through the porous NiFeOOH NSs/NF with airflow, and have a high probability of contact with the nanosheet surface due to intercept, impact, and Brownian motion. After approaching the surface of NiFeOOH NSs/NF, the sharp nanosheets structure of NiFeOOH NSs can scratch and insert bacterial cell membrane and cause physical destruction to bacteria [29]. When the light is involved in the system (PCO involved), photogenerated ROSs produced by the NiFeOOH NSs/NF/O_3 can directly attack bacterial cellular tissue. Meanwhile, the NiFeOOH NSs inserted inside the bacteria can provide a transport channel for photogenerated ROS migration into the bacteria, causing a fast oxidation within bacteria. Therefore, in the NiFeOOH NSs/NF/O_3 system under UV irradiation, physical destruction helps destroy bacterial cell membrane, promoting ROSs injecting into cells for fast and irreversible inactivation of bacteria. With the synergistic effect of oxidative damage caused by photogenerated ROSs and physical destruction caused by NiFeOOH NSs/NF, the NiFeOOH NSs/NF/O_3 system can inactivate bioaerosols efficiently and without the risk of secondary contaminant exposure.

4. Conclusion

In this work, NiFeOOH NSs successfully *in situ* grown on the surface of NF by a simple hydrothermal method. We have constructed a PCO system by combining of NiFeOOH NSs/NF photocatalyst and a trace of O_3, which showed 99.99% bacteria inactivation within retention time of 8.07 s. It has been found that introducing trace O_3 into NiFeOOH NSs/NF photocatalytic system can significantly enhance ROSs generation for bacteria inactivation due to high oxidation potential of O_3. Moreover, NiFeOOH NSs/NF with sharp nanosheets can enhance the bioaerosols inactivation efficiency by causing more serious physical destruction to bacteria, facilitating the injection of ROSs into bacteria. This synergistic effect of the physical destruction and ROSs oxidization further amplifies the destruction of the cell membrane and leads to the irreversible death of bacteria. This research provides a possible solution for the effective control of bioaerosols pollutants and expands new development directions for air purification technology.

CRediT authorship contribution statement

Haiyu Wang: Methodology, Formal analysis, Writing – original draft. **Linghui Peng:** Methodology, Data curation. **Guiying Li:** Writing – review & editing. **Weiping Zhang:** Visualization, Investigation. **Zhishu Liang:** Methodology, Validation. **Huijun Zhao:** Validation. **Taicheng An:** Conceptualization, Supervision.

Declaration of Competing Interest

The authors declare that they have no known competing financial interests or personal relationships that could have appeared to influence the work reported in this paper.

Data Availability

No data was used for the research described in the article.

Appendix A. Supporting information

Supplementary data associated with this article can be found in the online version at doi:10.1016/j.apcatb.2022.122273.

References

[1] B.J. Cowling, D.K.M. Ip, V.J. Fang, P. Suntarattiwong, S.J. Olsen, J. Levy, T. M. Uyeki, G.M. Leung, J.S. Malik Peiris, T. Chotpitayasunondh, H. Nishiura, J. Mark Simmerman, Aerosol transmission is an important mode of influenza A virus spread, Nat. Commun. 4 (2013) 1935.

[2] J. Douwes, P. Thorne, N. Pearce, D. Heederik, Bioaerosol health effects and exposure assessment: progress and prospects, Ann. Occup. Hyg. 47 (2003) 187–200.

[3] K. Bertran, C. Balzli, Y.K. Kwon, T.M. Tumpey, A. Clark, D.E. Swayne, Airborne transmission of highly pathogenic influenza virus during processing of infected poultry, Emerg. Infect. Dis. 23 (2017) 1806–1814.

[4] M.Z. Tay, C.M. Poh, L. Renia, P.A. MacAry, L.F.P. Ng, The trinity of COVID-19: immunity, inflammation and intervention, Nat. Rev. Immunol. 20 (2020) 363–374.

[5] N.C. Peeri, N. Shrestha, M.S. Rahman, R. Zaki, Z. Tan, S. Bibi, M. Baghbanzadeh, N. Aghamohammadi, W. Zhang, U. Haque, The SARS, MERS and novel coronavirus (COVID-19) epidemics, the newest and biggest global health threats: what lessons have we learned? Int. J. Epidemiol. 49 (2020) 717–726.

[6] W. Xie, Y. Li, W. Bai, J. Hou, T. Ma, X. Zeng, L. Zhang, T. An, The source and transport of bioaerosols in the air: a review, Front. Environ. Sci. Eng. 15 (2021) 44.

[7] F. Shen, D. Li, J. Chen, Mechanistic toxicity assessment of fine particulate matter emitted from fuel combustion via pathway-based approaches in human cells, Sci. Total. Environ. 806 (2022), 150214.

[8] W. Hu, K. Murata, C.L. Fan, S. Huang, H. Matsusaki, P.Q. Fu, D. Zhang, Abundance and viability of particle-attached and free-floatingbacteria in dusty and nondusty air, Biogeosciences 17 (2020) 4477–4487.

[9] N. Van Doremalen, T. Bushmaker, D.H. Morris, M.G. Holbrook, A. Gamble, B. N. Williamson, A. Tamin, J.L. Harcourt, N.J. Thornburg, S.I. Gerber, J.O. Lloyd Smith, E. de Wit, V.J. Munster, Aerosol and surface stability of SARS-CoV-2 as compared with SARS-CoV-1, N. Engl. J. Med 382 (2020) 1564–1567.

[10] V. Stadnytskyi, C.E. Bax, A. Bax, P. Anfinrud, The airborne lifetime of small speech droplets and their potential importance in SARS-CoV-2 transmission, P. Natl. Acad. Sci. 117 (2020) 11875–11877.

[11] W.Z. Chen, N. Zhang, J.J. Wei, H.L. Yen, Y.G. Li, Short-range airborne route dominates exposure of respiratory infection during close contact, Build. Environ. 176 (2020), 106859.

[12] L. Zhou, M. Yao, X. Zhang, B. Hu, X. Li, H. Chen, L. Zhang, Y. Liu, M. Du, B. Sun, Y. Jiang, K. Zhou, J. Hong, N. Yu, Z. Ding, Y. Xu, M. Hu, L. Morawska, S. A. Grinshpun, P. Biswas, R.C. Flagan, B. Zhu, W. Liu, Y. Zhang, Breath-, air- and surface-borne SARS-CoV-2 in hospitals, J. Aerosol Sci. 152 (2021), 105693.

[13] W. Wang, T.W. Ng, W.K. Ho, J. Huang, S. Liang, T. An, G. Li, J.C. Yu, P.K. Wong, CdIn$_2$S$_4$ microsphere as an efficient visible-light-driven photocatalyst for bacterial inactivation: Synthesis, characterizations and photocatalytic inactivation mechanisms, Appl. Catal. B: Environ. 129 (2013) 482–490.

[14] D. Wu, S. Yue, W. Wang, T. An, G. Li, H.Y. Yip, H.J. Zhao, P.K. Wong, Boron doped BiOBr nanosheets with enhanced photocatalytic inactivation of Escherichia coli, Appl. Catal. B: Environ. 192 (2016) 35–45.

[15] M. Li, M.E. Noriega Trevino, N. Nino Martinez, C. Marambio Jones, J. Wang, R. Damoiseaux, F. Ruiz, E.M.V. Hoek, Synergistic Bactericidal activity of Ag-TiO$_2$ nanoparticles in both light and dark conditions, Environ. Sci. Technol. 45 (2011) 8989–8995.

[16] P. Li, J. Li, X. Feng, J. Li, Y. Hao, J. Zhang, H. Wang, A. Yin, J. Zhou, X. Ma, B. Wang, Metal-organic frameworks with photocatalytic bactericidal activity for integrated air cleaning, Nat. Commun. 10 (2019) 2177.

[17] C. Rodrigues Silva, S.M. Miranda, F.V.S. Lopes, M. Silva, M. Dezotti, A.M.T. Silva, J.L. Faria, R.A.R. Boaventura, V.J.P. Vilar, E. Pinto, Bacteria and fungi inactivation by photocatalysis under UVA irradiation: liquid and gas phase, Environ. Sci. Pollut. Res. Int 24 (2017) 6372–6381.

[18] S. Lu, G. Meng, C. Wang, H. Chen, Photocatalytic inactivation of airborne bacteria in a polyurethane foam reactor loaded with a hybrid of MXene and anatase TiO₂ exposing {0 0 1} facets, Chem. Eng. J. 404 (2021), 126526.

[19] C.S. Uyguner Demirel, N.C. Birben, M. Bekbolet, A comprehensive review on the use of second generation TiO₂ photocatalysts: microorganism inactivation, Chemosphere 211 (2018) 420–448.

[20] S. Josset, S. Hajiesmaili, D. Begin, D. Edouard, C. Pham-Huu, M.C. Lett, N. Keller, V. Keller, UV-A photocatalytic treatment of Legionella pneumophila bacteria contaminated airflows through three-dimensional solid foam structured photocatalytic reactors, J. Hazard. Mater. 175 (2010) 372–381.

[21] M. Wang, M. Ateia, D. Awfa, C. Yoshimura, Regrowth of bacteria after light-based disinfection — what we know and where we go from here, Chemosphere 268 (2021), 128850.

[22] F. Biancullo, N.F.F. Moreira, A.R. Ribeiro, C.M. Manaia, J.L. Faria, O.C. Nunes, S. M. Castro-Silva, A.M.T. Silva, Heterogeneous photocatalysis using UVA-LEDs for the removal of antibiotics and antibiotic resistant bacteria from urban wastewater treatment plant effluents, Chem. Eng. J. 367 (2019) 304–313.

[23] Y. Li, W. Zhang, J. Niu, Y. Chen, Mechanism of photogenerated reactive oxygen species and correlation with the antibacterial properties of engineered metal-oxide nanoparticles, ACS Nano 6 (2012) 5164–5173.

[24] U. Joost, K. Juganson, M. Visnapuu, M. Mortimer, A. Kahru, E. Nommiste, U. Joost, V. Kisand, A. Ivask, Photocatalytic antibacterial activity of nano-TiO₂ (anatase)-based thin films: effects on Escherichia coli cells and fatty acids, J. Photochem. Photobiol. B 142 (2015) 178–185.

[25] Y. Nosaka, A.Y. Nosaka, Generation and detection of reactive oxygen species in photocatalysis, Chem. Rev. 117 (2017) 11302–11336.

[26] N.F.F. Moreira, J.M. Sousa, G. Macedo, A.R. Ribeiro, L. Barreiros, M. Pedrosa, J. L. Faria, M.F.R. Pereira, S. Castro-Silva, M.A. Segundo, C.M. Manaia, O.C. Nunes, A.M.T. Silva, Photocatalytic ozonation of urban wastewater and surface water using immobilized TiO₂ with LEDs: micropollutants, antibiotic resistance genes and estrogenic activity, Water Res. 94 (2016) 10–22.

[27] A.C. Mecha, M.S. Onyango, A. Ochieng, M.N.B. Momba, Evaluation of synergy and bacterial regrowth in photocatalytic ozonation disinfection of municipal wastewater, Sci. Total. Environ., 601- 602 (2017) 626–635.

[28] N. Lin, P. Berton, C. Moraes, R.D. Rogers, N. Tufenkji, Nanodarts, nanoblades, and nanospikes: mechano-bactericidal nanostructures and where to find them, Adv. Colloid Interface Sci. 252 (2018) 55–68.

[29] K. Modaresifar, S. Azizian, M. Ganjian, L.E. Fratila-Apachitei, A.A. Zadpoor, Bactericidal effects of nanopatterns: a systematic review, Acta Biomater. 83 (2019) 29–36.

[30] D.P. Linklater, M. De Volder, V.A. Baulin, M. Werner, S. Jessl, M. Golozar, L. Maggini, S. Rubanov, E. Hanssen, S. Juodkazis, E.P. Ivanova, High aspect ratio nanostructures kill bacteria via storage and release of mechanical energy, ACS Nano 12 (2018) 6657–6667.

[31] J. Jenkins, J. Mantell, C. Neal, A. Gholinia, P. Verkade, A.H. Nobbs, B. Su, Antibacterial effects of nanopillar surfaces are mediated by cell impedance, penetration and induction of oxidative stress, Nat. Commun. 11 (2020) 1626.

[32] L.M. Gilbertson, E.M. Albalghiti, Z.S. Fishman, F. Perreault, C. Corredor, J. D. Posner, M. Elimelech, L.D. Pfefferle, J.B. Zimmerman, Shape-dependent surface reactivity and antimicrobial activity of nano-cupric oxide, Environ. Sci. Technol. 50 (2016) 3975–3984.

[33] H. He, P. Zhou, K.K. Shimabuku, X. Fang, S. Li, Y. Lee, M.C. Dodd, Degradation and deactivation of bacterial antibiotic resistance genes during exposure to free chlorine, monochloramine, chlorine dioxide, ozone, ultraviolet light, and hydroxyl radical, Environ. Sci. Technol. 53 (2019) 2013–2026.

[34] J.D. Xiao, J. Rabeah, J. Yang, Y.B. Xie, H.B. Cao, A. Bruckner, Fast electron transfer and (OH)-O-center dot formation: key features for high activity in visible-light-driven ozonation with C₃N₄ catalysts, ACS Catal. 7 (2017) 6198–6206.

[35] L. Dong, Y. Liu, Y. Lu, L. Zhang, N. Man, L. Cao, K. Ma, D. An, J. Lin, Y.J. Xu, W. P. Xu, W.B. Wu, S.H. Yu, L.P. Wen, Tuning magnetic property and autophagic response for self-assembled Ni-Co alloy nanocrystals, Adv. Funct. Mater. 23 (2013) 5930–5940.

[36] L. Wang, C. Ye, L. Guo, C. Chen, Y. Kong, Y. Chen, L. Shu, P. Wang, X. Yu, J. Fang, Assessment of the UV/chlorine process in the disinfection of pseudomonas aeruginosa: efficiency and mechanism, Environ. Sci. Technol. 55 (2021) 9221–9230.

[37] W. Fei, J. Gao, N. Li, D. Chen, Q. Xu, H. Li, J. He, J. Lu, A visible-light active p-n heterojunction NiFe-LDH/Co₃O₄ supported on Ni foam as photoanode for photoelectrocatalytic removal of contaminants, J. Hazard. Mater. 402 (2021), 123515.

[38] L.Y. Hu, X. Zeng, X.Q. Wei, H.J. Wang, Y. Wu, W.L. Gu, L. Shi, C.Z. Zhu, Interface engineering for enhancing electrocatalytic oxygen evolution of NiFe LDH/NiTe heterostructures, Appl. Catal. B: Environ. 273 (2020) 119014.

[39] D. Chen, Z. Liu, S. Zhang, Enhanced PEC performance of hematite photoanode coupled with bimetallic oxyhydroxide NiFeOOH through a simple electroless method, Appl. Catal. B: Environ. 265 (2020) 118580.

[40] M.P. Suryawanshi, S.W. Shin, U.V. Ghorpade, J. Kim, H.W. Jeong, S.H. Kang, J. H. Kim, A facile, one-step electroless deposition of NiFeOOH nanosheets onto photoanodes for highly durable and efficient solar water oxidation, J. Mater. Chem. A 6 (2018) 20678–20685.

[41] J. Kim, J. Jang, Inactivation of airborne viruses using vacuum ultraviolet photocatalysis for a flow-through indoor air purifier with short irradiation time, Aerosol Sci. Technol. 52 (2018) 557–566.

[42] F. Wang, J. Dai, L. Huang, Y. Si, J. Yu, B. Ding, Biomimetic and superelastic silica nanofibrous aerogels with rechargeable bactericidal function for antifouling water disinfection, ACS Nano 14 (2020) 8975–8984.

[43] C.C. Tseng, C.S. Li, Ozone for inactivation of aerosolized bacteriophages, Aerosol Sci. Technol. 40 (2006) 683–689.

[44] X. He, X. Liu, P. Li, P. Wang, H. Cheng, W. Li, B. Li, T. Liu, J. Ma, A multi-stage green barrier strategy for the control of global SARS-CoV-2 transmission via cold chain goods, Engineering 9 (2021) 13–16.

[45] J.B. Hudson, M. Sharma, S. Vimalanathan, Development of a practical method for using ozone gas as a virus decontaminating agent, Ozone-Sci. Eng. 31 (2009) 216–223.

[46] L. Liu, G. Meng, A.A. Laghari, H. Chen, C. Wang, Y. Xue, Reducing the risk of exposure of airborne antibiotic resistant bacteria and antibiotic resistance genes by dynamic continuous flow photocatalytic reactor, J. Hazard. Mater. 429 (2022), 128311.

[47] Z. Teng, N. Yang, H. Lv, S. Wang, M. Hu, C. Wang, D. Wang, G. Wang, Edge-functionalized g-C₃N₄ nanosheets as a highly efficient metal-free photocatalyst for safe drinking water, Chem 5 (2019) 664–680.

[48] J. Xiao, Q. Han, Y. Xie, J. Yang, Q. Su, Y. Chen, H. Cao, Is C₃N₄ chemically stable toward reactive oxygen species in sunlight-driven water treatment? Environ. Sci. Technol. 51 (2017) 13380–13387.

[49] F. Perreault, A.F. de Faria, S. Nejati, M. Elimelech, Antimicrobial properties of graphene oxide nanosheets: why size matters, ACS Nano 9 (2015) 7226–7236.

[50] I.C. Iakovides, K. Manoli, P. Karaolia, I. Michael-Kordatou, C.M. Manaia, D. Fatta-Kassinos, Reduction of antibiotic resistance determinants in urban wastewater by ozone: emphasis on the impact of wastewater matrix towards the inactivation kinetics, toxicity and bacterial regrowth, J. Hazard. Mater. 15 (2021), 126527.

[51] J. Alexander, G. Knopp, A. Dötsch, A. Wieland, T. Schwartz, Ozone treatment of conditioned wastewater selects antibiotic resistance genes, opportunistic bacteria, and induce strong population shifts, Sci. Total. Environ. 559 (2016) 103–112.